Propagating helical waves as a building block of round turbulent jets

Mullyadzhanov, R. I.; Sandberg, R. D.; Abdurakipov, S. S.; George, W. K.; Hanjalić, K.

DOI
10.1103/PhysRevFluids.3.062601

Publication date
2018

Document Version
Final published version

Published in
Physical Review Fluids

Rapid Communications

Propagating helical waves as a building block of round turbulent jets

R. I. Mullyadzhanov,[1,2,*] R. D. Sandberg,[3] S. S. Abdurakipov,[1,2] W. K. George,[4] and K. Hanjalić[2,5]
[1]*Institute of Thermophysics SB RAS, Lavrentyeva 1, Novosibirsk 630090, Russia*
[2]*Novosibirsk State University, Pirogova 2, Novosibirsk 630090, Russia*
[3]*University of Melbourne, Victoria 3010, Australia*
[4]*Imperial College of Science, Technology and Medicine, London SW7 2AZ, United Kingdom*
[5]*Delft University of Technology, Building 58, Van der Maasweg 9, 2629 HZ Delft, The Netherlands*

(Received 21 February 2017; published 14 June 2018)

Turbulent jets are known to support large-scale vortical wave packets traveling downstream. We show that a propagating helical wave represents a common form of the "optimal" eigenfunction tracking these structures from the near to the far field of a round jet issuing from a pipe. Two first mirror-symmetric modes containing around 5% of the total turbulent kinetic energy capture all significant large-scale events and accurately replicate the full shear-layer dynamics of the azimuthal wave number $m = 1$. A family of the most energy-containing traveling waves represents low wave numbers and is described in terms of "empirical" dispersion laws.

DOI: 10.1103/PhysRevFluids.3.062601

Large-scale organized (coherent) vortical structures are at the heart of free-shear turbulent flows, such as wakes, mixing layers, and jets [1,2]. These structures are involved in intensive mixing and entrainment [3] and play a significant role in the generation of aeroacoustic noise [4]. Vortical dynamics is extremely sensitive to initial and/or boundary conditions [5–11] and defines the asymptotic self-similar flow states at larger evolution times or distances [12–16]. Optimal control routes require a deep understanding of spatial and dynamical flow organization with coherent vortices representing the energetic backbone.

For a round transitional jet, this vortical "skeleton" usually appears as Kelvin-Helmholtz rings near the nozzle while further downstream they break down, producing fully developed turbulent flow [17]. Previous observations [18–23] suggest the presence of helical structures in the fully developed region with various azimuthal wave numbers m. These waves ("wave packets") are usually treated by using a linearized framework or using reduced-order modeling [24–33]. While close to the nozzle this approach is successful, a full understanding of wavy motion and a corresponding dispersion law in the far jet is still lacking.

In this Rapid Communication, we analyze direct numerical simulation data of a turbulent jet [34], performed with an in-house high-order finite-difference/pseudospectral code that solves the compressible Navier-Stokes equations using 400 million grid points. We consider a jet at Reynolds number $\mathrm{Re} = 5940$ based on the bulk velocity U_b in the pipe and its diameter D generated by a fully turbulent pipe flow entering a uniform stream with a coflow velocity $u_{\mathrm{co}} = 0.27U_b$. Together with a sufficient spatial resolution, the computation features a very long time realization with around $400D/U_b$ time units, allowing one to statistically assess even the far field of the jet.

A visual impression of the turbulent dynamics is given by the instantaneous vorticity magnitude field, shown in Fig. 1(a). While the simulation area includes $x = 50D$, the analyzed physical region covers only the domain up to $x \leqslant 40D$ to avoid the influence of the outflow boundary conditions

*rustammul@gmail.com

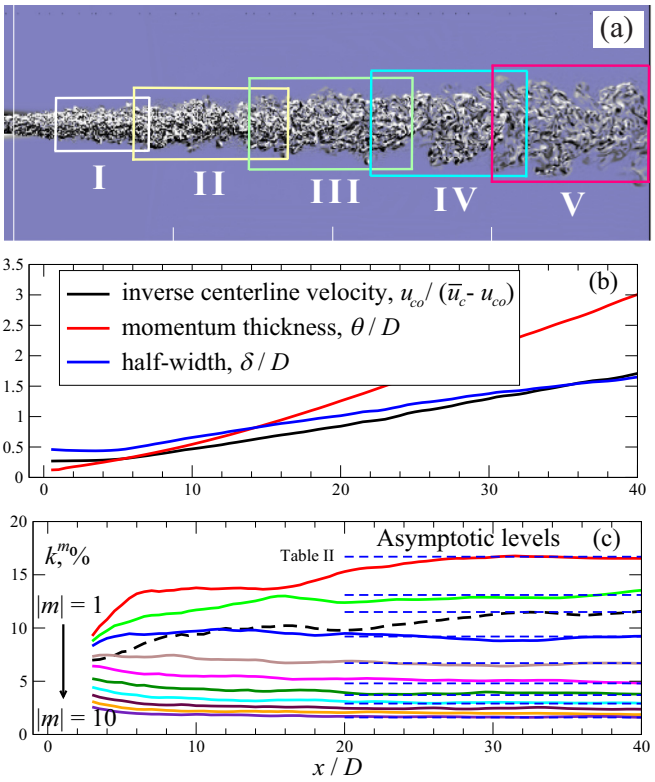

FIG. 1. (a) Instantaneous contours of the vorticity field and five subdomains for further statistical analysis. (b) $u_{\rm co}/(\overline{u}_c - u_{\rm co})$, θ, and δ against x/D. (c) Cross-section integrated kinetic energy for azimuthal wave numbers; the black dashed line shows $m = 0$. The momentum thickness is defined as $\theta = 2D^{-1}\int \overline{u}_{x,n}(1 - \overline{u}_{x,n})rdr$, where $\overline{u}_{x,n} = (\overline{u}_x - u_{\rm co})/(\overline{u}_c - u_{\rm co})$. The local half width is defined as the point $r = \delta$ where the time-averaged axial velocity is half the value of the sum $\overline{u}_c + u_{\rm co}$. Horizontal blue dashed lines show the "asymptotic" levels of energy for each m (see Table II).

(see Ref. [34]). Five cylindrical subdomains in the flow field are highlighted, denoting where the subsequent statistical analysis is performed (see Table I). The time-averaged center-line velocity $\overline{u}_c$, momentum thickness θ, and half width of the jet δ are shown in Fig. 1(b) against the downstream distance, indicating that fully developed (self-similar) flow is achieved after around $x = 20D$.

TABLE I. Geometrical characteristics of domains I–V shown in Fig. 1(a) with x_s,x_e being the axial coordinates of the bottom and top, and R the radius of each cylindrical subdomain.

Domain	x_s/D	x_e/D	R/D
I	2.5	8.5	1.5
II	7.5	17.5	2.0
III	15.0	25.0	2.5
IV	22.5	32.5	2.8
V	30.0	40.0	3.0

TABLE II. Asymptotic levels of turbulent kinetic energy in the far jet for different azimuthal wave numbers [see Fig. 1(c)].

$\|m\|$	0	1	2	3	4	5	6	7	8	9	10
k^m (%)	11.5	16.7	13.1	9.2	6.7	4.8	3.7	2.9	2.4	1.9	1.6

The round geometry suggests Fourier decomposition in the azimuthal direction ϕ with complex coefficients representing the velocity field $\boldsymbol{u}$,

$$\boldsymbol{u}(r,x,m,t) = \boldsymbol{u}^m = \frac{1}{2\pi}\int_0^{2\pi} \boldsymbol{u}(r,x,\phi,t)e^{im\phi}d\phi. \tag{1}$$

The turbulent kinetic energy of each azimuthal mode, $k^m = |\boldsymbol{u}^m|^2/2$, integrated over the r-ϕ plane, is shown in Fig. 1(c). Close to the inflow, due to the exit of fully developed pipe turbulence, a broad spectrum of high m modes is excited while further downstream low wave numbers carry the bulk of the energy with some "asymptotic" levels reached at $x = 40D$ (see Table II).

We further apply snapshot proper orthogonal decomposition (POD) [35] for each azimuthal wave number m and each cylindrical subdomain I–V to an ensemble of Fourier-decomposed fields $[\boldsymbol{u}_1^m, \boldsymbol{u}_2^m, \ldots, \boldsymbol{u}_N^m]$ corresponding to subsequent time instants $t = t_1, \ldots, t_N$,

$$\boldsymbol{u}_i^m(r,x) = \boldsymbol{u}(r,x,m,t_i) = \sum_{q=1}^{N} a_q^m(t_i)\lambda_q^m \boldsymbol{v}_q^m(r,x), \tag{2}$$

where $\boldsymbol{v}_q^m(r,x)$ and $a_q^m(t)$ are the nondimensional complex-valued spatial eigenfunctions and temporal amplitudes satisfying orthonormal conditions [36,37], λ_q^m are the real eigenvalues.

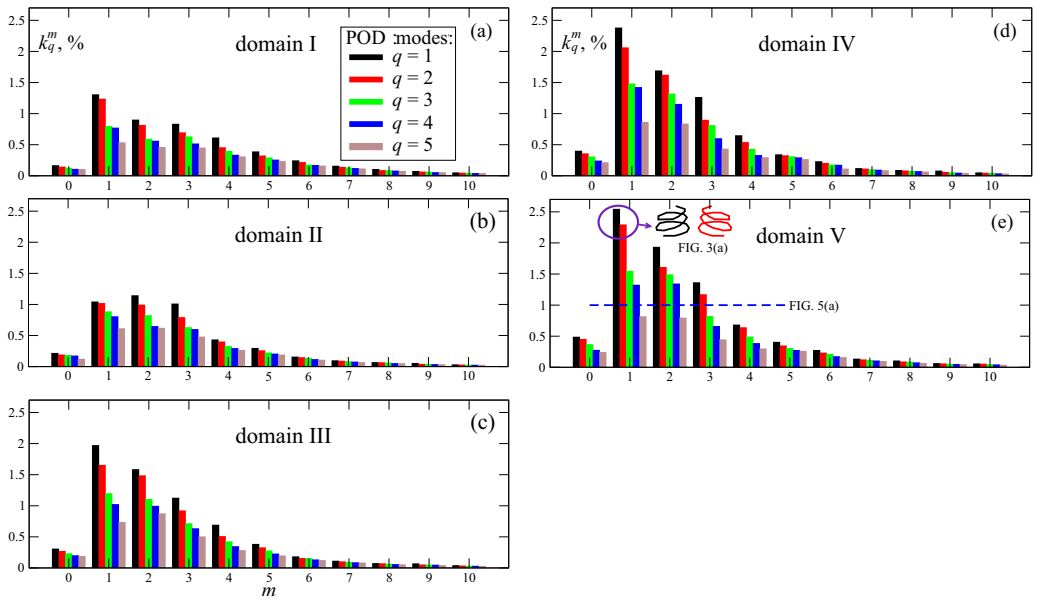

FIG. 2. Distribution of $k_q^m = (\lambda_q^m)^2/2$ (normalized by the total energy in a particular domain) among the most energetic POD modes for various m and domains I–V. The index q denotes the number of ranked modes according to the value of k_q^m.

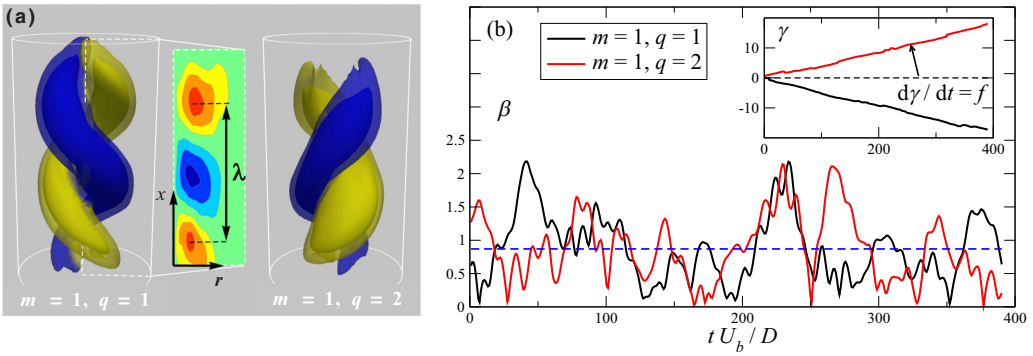

FIG. 3. (a) Isosurface of the velocity magnitude colored with axial velocity for $m = 1$ and $q = 1,2$ for domain V. Contour plot shows the real part of the POD axial velocity field. (b) Evolution of β and γ calculated for $a^{m=1}_{q=1,2}$ in domain V.

Figure 2 shows the turbulent kinetic energy $k^m_q = (\lambda^m_q)^2/2$ of the most energetic POD modes for various m and different domains. As noted above, the self-similar jet area is governed by energy-containing modes with low m compared to the near field. The eigenfunctions come in pairs of (virtually) equal amounts of energy which is especially evident in the near field where the time realization is extremely long in terms of the local timescales, providing well-converged results. Each mode should have a counterpart identical with respect to $\phi \to -\phi$ symmetry as a consequence of round geometry and the absence of mean swirl. Figure 3(a) shows the helical shape of the two most energetic modes with $m = 1$ and $q = 1,2$ in domain V which together provide 4.85% of the total energy. The helix is formed due to the wavelike distribution of $\boldsymbol{v}^m_q(r,x)$ in the x direction, together with the Fourier decomposition with respect to ϕ. This shape is observed for all energetic modes and can be interpreted as the common form of the basis jet eigenfunction ("optimal" in terms of POD).

To probe the dynamical features of these helices we analyze the complex-valued temporal amplitudes a^m_q starting with the representation $a(t) = \beta(t)e^{2\pi i\gamma(t)}$, where β and γ are real functions of time. An important observation is that γ turns out to be a linear function, $\gamma \approx ft$; see the inset on Fig. 3(b) [38,39]. Note that the matching mirror modes have the same value of γ but opposite signs corresponding to the rotation of the helices around the axis of symmetry in the opposite direction, with f being the frequency of rotation. The revealed $e^{2\pi ift}$ dependence implies that the described helices travel (propagate) downstream with a phase velocity as defined below. Turbulence dynamics is represented by the amplitude β (Fig. 3), where their large-scale fluctuations also appear with the period of the helix rotation $1/f \approx 22.5D/U_b$ or $\approx 5.6\delta/\overline{u}_x$ using the local scaling at $x = 35D$ and $r = \delta$.

The properties of the helical wave corresponding to the most energetic POD mode with $m = 1$ are summarized in Figs. 4(a) and 4(b). The frequency decays with x but also fluctuates around a constant value of 0.17 when normalized with the local jet characteristics. The propagation or phase velocity defined as $u_{\mathrm{ph}} = f\lambda$ is slightly lower than 1.0 in terms of δ and $\overline{u}_x(\delta)$, in agreement with previous findings [40]. The POD results extracted from the direct numerical simulation (DNS) data are compared with the local linear spatial stability analysis that uses a quasiparallel assumption based on the time-averaged velocity profiles. The linearized equations for the coherent part of perturbations $\widetilde{\boldsymbol{u}}$ are derived with the perturbation represented as a monochromatic wave, i.e., $\widetilde{\boldsymbol{u}} = \hat{\boldsymbol{u}}(r)e^{ik_x x + im\phi - 2\pi ift}$, where $k_x = k^{re}_x + ik^{im}_x$ is the complex-valued streamwise wave number, with $k^{re}_x = 2\pi/\lambda$. The Reynolds stresses are modeled using the Boussinesq approximation. These equations result in a system of linear ordinary differential equations (ODEs), with appropriate boundary conditions which are solved for the unknown function $\hat{\boldsymbol{u}}$ providing the dispersion relation $k_x = k_x(f)$ (see the Supplemental Material [36]). A disturbance is exponentially amplified at a given real frequency f provided that $k^{im}_x(f) < 0$. The only unstable azimuthal mode is $m = 1$ with f and u_{ph} of the neutral

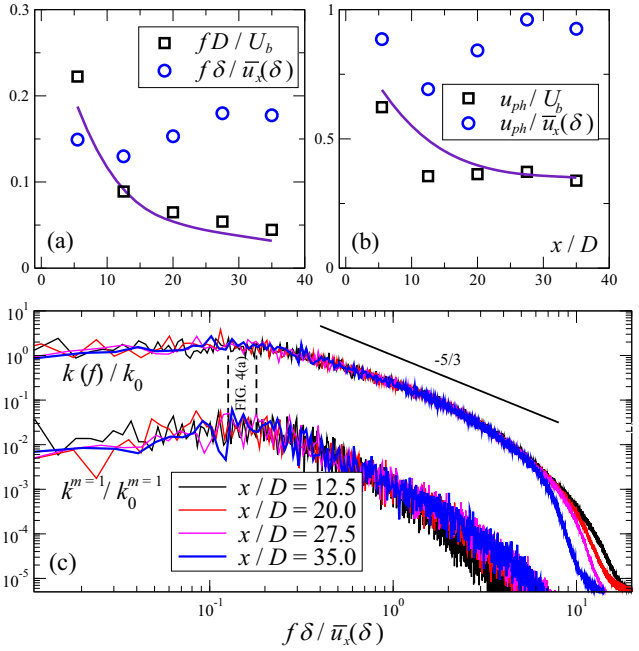

FIG. 4. (a), (b) Variation of f and $u_{\rm ph}$ with x. Symbols: POD normalized with U_b, D (squares) and local values $\delta, \overline{u}_x(r=\delta)$ (circles); line: linear stability analysis (U_b, D). (c) Normalized total turbulent kinetic energy spectra $k(f)$ in the shear layer, $r=\delta$, and different axial positions together with the normalized spectra for $m=1$, $k^{m=1}$ (shifted down for clarity).

eigensolution ($k_x^{im}=0$) presented in Figs. 4(a) and 4(b) showing a close resemblance with the POD results. Further, we assess the normalized turbulent kinetic energy spectrum $k(f)$ in the shear layer at different axial positions, shown in Fig. 4(c). Note the evident self-similarity of large scales as the individual spectra collapse on a single curve [41]. Vertical dashed lines show the frequency scatter depicted in Fig. 4(a) residing near the inertial range where the dynamics of POD modes with $m=1$ and $q=1,2$ is expected to contribute. This range is indeed the most energy containing, with 43% of the total energy in the low-frequency range up to $f\delta/\overline{u}_x < 0.24$. The spectra of $k^{m=1}$ show a distinct bump in this range of frequencies. For the spectral analysis of a broader range of m, see the Supplemental Material [36].

One may ask if the identified most energetic coherent structures are of dynamical significance. Figure 5(a) shows comparison of instantaneous streamwise velocity fluctuations at $x=35D$ in the

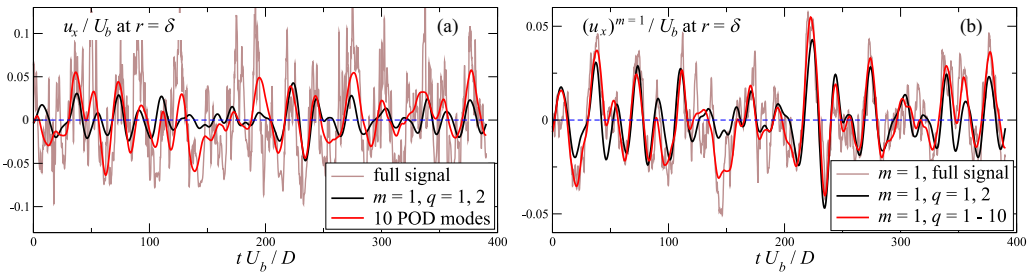

FIG. 5. Comparison of streamwise velocity fluctuation signal at $x=35D$, $r=\delta$ with that recovered from POD for (a) the full signal and (b) $m=1$ only.

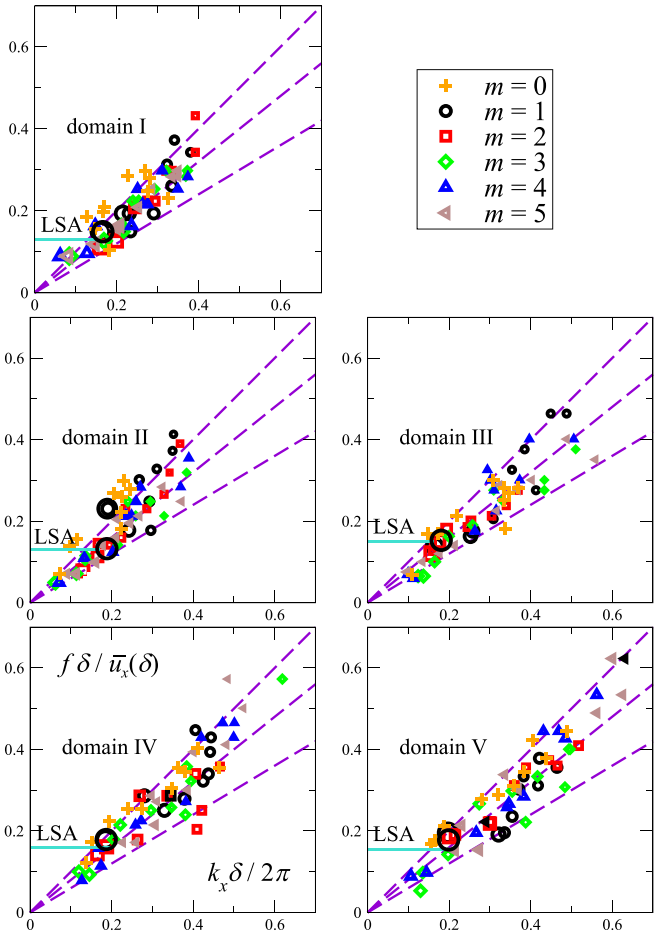

FIG. 6. The diagram of the most energetic POD modes with various m and q indices in k_x-f space normalized with local characteristics ($f\delta/\overline{u}_x$ against $k_x\delta/2\pi$). Each symbol represents a separate mode while the size of the symbol schematically shows the amount of energy represented by this mode (Fig. 2). The axial wavelength ($\lambda = 2\pi/k_x$) and frequency ($f = d\gamma/dt$) are extracted for each q and m according to Fig. 3. Three dashed lines denote the phase velocities ($u_{\mathrm{ph}}/\overline{u}_x$) of 0.6, 0.8, and 1.0, respectively. The horizontal line shows the results of linear stability analysis (LSA) [Fig. 4(a)].

shear layer with that provided by the reduced-order POD model recovered using a different number of modes. Two modes with $m = 1$ and $q = 1,2$ representing only 4.85% of total energy capture all significant large-scale events. The ten most energetic modes with $m = 1$, 2, and 3 [see Fig. 2(e)], containing 16.66% of the overall energy, sufficiently improve the amplitude of the signal. If one inspects only the $m = 1$ instantaneous signal of the streamwise velocity fluctuations, these two modes $q = 1,2$ are sufficient to replicate the full signal with high accuracy [Fig. 5(b)], confirming the significance of the identified structures. Similar results are also found for other m.

We have documented in detail the most energetic mode with $m = 1$ and $q = 1,2$ while the overall dynamics can be fairly represented by a family of traveling waves (Fig. 5). To get a general view of the spatiotemporal properties of wavy motion we plot an "empirical" dispersion law as a diagram in k_x-f space (Fig. 6; see also Ref. [42]). Symbols represent separate POD modes with their respective amount of energy, spatial, and spectral features, extracted according to Fig. 3 with a specific axial wavelength ($\lambda = 2\pi/k_x$) and frequency ($f = d\gamma/dt$) for each q and m. While structures with $m > 0$

behave similarly in the near and far field, axisymmetric modes have higher phase velocities close to the nozzle, governed by a Kelvin-Helmholtz instability. When reaching the far jet, the phase velocity for $m = 0$ can be confidently bounded in the interval $0.8 < u_{\mathrm{ph}}/\overline{u}_x < 1.0$ while $u_{\mathrm{ph}}/\overline{u}_x$ for waves with $m > 0$ vary from 0.6 to 1.0 [43].

Thus, we have shown that propagating waves are the building units of the "optimal" basis (the feature of POD) describing the dynamics of turbulent jets. We tracked the wave packets from the near to the far field and showed their scaling properties and dispersion laws in terms of local jet characteristics. According to far-jet asymptotics, this dynamical "skeleton" is expected to be universal also for swirling and nonaxisymmetric jets [44]. Future work should demonstrate the particular role of the observed structures and their contribution to mixing [21], aeroacoustics [45], and to the strong anisotropy and peculiarities of the concentration distribution in particle-laden jets [46]. The obtained basis can also be a good candidate for a Craya-type decomposition for inhomogeneous flows to inspect the role of helicity in the energy transfer [47–49].

This work is funded by the Russian Science Foundation Grant No. 14-19-01685. The resources for postprocessing are provided by Novosibirsk State University supercomputer center, Siberian Supercomputer Center SB RAS (Novosibirsk) and Joint Supercomputer Center RAS (Moscow). The authors are grateful to the anonymous referees for their valuable comments.

[1] B. J. Cantwell, Organized motion in turbulent flow, Annu. Rev. Fluid Mech. **13**, 457 (1981).
[2] A. K. M. F. Hussain, Coherent structures – reality and myth, Phys. Fluids **26**, 2816 (1983).
[3] C. G. Ball, H. Fellouah, and A. Pollard, The flow field in turbulent round free jets, Prog. Aerosp. Sci. **50**, 1 (2012).
[4] P. Jordan and T. Colonius, Wave packets and turbulent jet noise, Annu. Rev. Fluid Mech. **45**, 173 (2013).
[5] S. C. Crow and F. H. Champagne, Orderly structure in jet turbulence, J. Fluid Mech. **48**, 547 (1971).
[6] K. B. M. Q. Zaman and A. K. M. F. Hussain, Turbulence suppression in free shear flows by controlled excitation, J. Fluid Mech. **103**, 133 (1981).
[7] E. Gutmark and C. M. Ho, Preferred modes and the spreading rates of jets, Phys. Fluids **26**, 2932 (1983).
[8] R. A. Antonia and Q. Zhao, Effect of initial conditions on a circular jet, Exp. Fluids **31**, 319 (2001).
[9] G. Xu and R. A. Antonia, Effect of different initial conditions on a turbulent round free jet, Exp. Fluids **33**, 677 (2002).
[10] J. Mi, D. S. Nobes, and G. J. Nathan, Influence of jet exit conditions on the passive scalar field of an axisymmetric free jet, J. Fluid Mech. **432**, 91 (2001).
[11] W. K. George, Asymptotic effect of initial and upstream conditions on turbulence, J. Fluids Eng. **134**, 061203 (2012).
[12] I. Wygnanski, F. Champagne, and B. Marasli, On the large-scale structures in two-dimensional, small-deficit, turbulent wakes, J. Fluid Mech. **168**, 31 (1986).
[13] W. K. George, The self-preservation of turbulent flows and its relation to initial conditions and coherent structures, in *Advances in Turbulence*, edited by W. K. George and R. Arndt (Hemisphere, New York, 1989), p. 39.
[14] P. B. Johansson, W. K. George, and M. J. Gourlay, Equilibrium similarity, effects of initial conditions and local Reynolds number on the axisymmetric wake, Phys. Fluids **15**, 603 (2003).
[15] J. P. Hickey, F. Hussain, and X. Wu, Role of coherent structures in multiple self-similar states of turbulent planar wakes, J. Fluid Mech. **731**, 312 (2013).
[16] M. Obligado, T. Dairay, and J. C. Vassilicos, Nonequilibrium scalings of turbulent wakes, Phys. Rev. Fluids **1**, 044409 (2016).
[17] A. J. Yule, Large-scale structure in the mixing layer of a round jet, J. Fluid Mech. **89**, 413 (1978).
[18] G. K. Batchelor and A. E. Gill, Analysis of the stability of axisymmetric jets, J. Fluid Mech. **14**, 529 (1962).

[19] I. Danaila, J. Dusek, and F. Anselmet, Coherent structures in a round, spatially evolving, unforced, homogeneous jet at low Reynolds numbers, Phys. Fluids **9**, 3323 (1997).
[20] P. E. Dimotakis, R. C. Miake-Lye, and D. A. Papantoniou, Structure and dynamics of round turbulent jets, Phys. Fluids **26**, 3185 (1983).
[21] J. Tso and F. Hussain, Organized motions in a fully developed turbulent axisymmetric jet, J. Fluid Mech. **203**, 425 (1989).
[22] A. Agrawal and A. K. Prasad, Organizational modes of large-scale vortices in an axisymmetric turbulent jet, Flow Turbul. Combust. **68**, 359 (2002).
[23] D. Jung, S. Gamard, and W. K. George, Downstream evolution of the most energetic modes in a turbulent axisymmetric jet at high Reynolds number. Part 1. The near-field region, J. Fluid Mech. **514**, 173 (2004).
[24] T. Suzuki and T. Colonius, Instability waves in a subsonic round jet detected using a near-field phased microphone array, J. Fluid Mech. **565**, 197 (2006).
[25] P. K. Ray, L. C. Cheung, and S. K. Lele, On the growth and propagation of linear instability waves in compressible turbulent jets, Phys. Fluids **21**, 054106 (2009).
[26] K. Gudmundsson and T. Colonius, Instability wave models for the near-field fluctuations of turbulent jets, J. Fluid Mech. **689**, 97 (2011).
[27] X. Garnaud, L. Lesshafft, P. J. Schmid, and P. Huerre, The preferred mode of incompressible jets: Linear frequency response analysis, J. Fluid Mech. **716**, 189 (2013).
[28] X. Garnaud, L. Lesshafft, P. J. Schmid, and P. Huerre, Modal and transient dynamics of jet flows, Phys. Fluids **25**, 044103 (2013).
[29] A. V. G. Cavalieri, D. Rodriguez, P. Jordan, T. Colonius, and Y. Gervais, Wavepackets in the velocity field of turbulent jets, J. Fluid Mech. **730**, 559 (2013).
[30] X. Garnaud, R. D. Sandberg, and L. Lesshafft, Global response to forcing in a subsonic jet: Instability wavepackets and acoustic radiation, in *19th AIAA/CEAS Aeroacoustics Conference, Aeroacoustics Conferences, Berlin, Germany* (AIAA, Reston, VA, 2013), paper AIAA 2013–2232.
[31] J. Ryu, S. K. Lele, and K. Viswanathan, Study of supersonic wave components in high-speed turbulent jets using an LES database, J. Sound Vibr. **333**, 6900 (2014).
[32] O. Semeraro, F. Lusseyran, L. Pastur, and P. Jordan, Qualitative dynamics of wave packets in turbulent jets, Phys. Rev. Fluids **2**, 094605 (2017).
[33] J. Jeun, J. W. Nichols, and M. R. Jovanovich, Input-output analysis of high-speed axisymmetric isothermal jet noise, Phys. Fluids **28**, 047101 (2016).
[34] R. D. Sandberg, N. D. Sandham, and V. Suponitsky, DNS of compressible pipe flow exiting into a coflow, Int. J. Heat Fluid Flow **35**, 33 (2012); M46-c1 case is used in the present work.
[35] L. Sirovich, Turbulence and the dynamics of coherent structures, I. Coherent structures, Q. Appl. Math. **45**, 561 (1987).
[36] See the Supplemental Material at http://link.aps.org/supplemental/10.1103/PhysRevFluids.3.062601 for POD details, additional calculations, the linear stability analysis framework, and a comparison of spectra for different azimuthal wave numbers m.
[37] R. Mullyadzhanov, S. Abdurakipov, and K. Hanjalic, Helical structures in the near field of a turbulent pipe jet, Flow Turbul. Combust. **98**, 367 (2017).
[38] L. Sirovich, K. S. Ball, and L. R. Keefe, Plane waves and structures in turbulent channel flow, Phys. Fluids A **2**, 2217 (1990).
[39] A. Duggleby, K. S. Ball, M. R. Paul, and P. F. Fischer, Dynamical eigenfunction decomposition of turbulent pipe flow, J. Turbul. **8**, N43 (2007).
[40] I. Wygnanski and H. Fiedler, Some measurements in the self-preserving jet, J. Fluid Mech. **38**, 577 (1969).
[41] P. Burattini, R. A. Antonia, and L. Danaila, Similarity in the far field of a turbulent round jet, Phys. Fluids **17**, 025101 (2005).
[42] O. T. Schmidt, A. Towne, G. Rigas, T. Colonius, and G. Brès, Spectral analysis of jet turbulence, arXiv:1711.06296.
[43] O. A. Likhachev, Analysis of stability in a self-similar circular jet with consideration of the nonparallel effect, J. Appl. Mech. Tech. Phys. **31**, 621 (1990).

[44] R. I. Mullyadzhanov and N. I. Yavorskii, Solution of the problem of flow of a non-axisymmetric swirling submerged jet, J. Appl. Mech. Tech. Phys. **54**, 207 (2013).
[45] Z. Fu, A. Agarwal, A. V. G. Cavalieri, P. Jordan, and G. Brès, Turbulent jet noise in the absence of coherent structures, Phys. Rev. Fluids **2**, 064601 (2017).
[46] T. C. Lau and G. J. Nathan, The effect of Stokes number on particle velocity and concentration distributions in a well-characterised, turbulent, co-flowing two-phase jet, J. Fluid Mech. **809**, 72 (2016).
[47] L. Biferale, S. Mussachio, and F. Toschi, Split energy-helicity cascades in three-dimensional homogeneous and isotropic turbulence, J. Fluid Mech. **730**, 309 (2013).
[48] M. Kessar, F. Plunian, R. Stepanov, and G. Balarac, Non-Kolmogorov cascade of helicity-driven turbulence, Phys. Rev. E **92**, 031004 (2015).
[49] A. Alexakis, Helically decomposed turbulence, J. Fluid Mech. **812**, 752 (2017).